Original Article

Chemical solution deposition of epitaxial indium- and aluminum-doped Ga_2O_3 thin films on sapphire with tunable bandgaps

Xiao Tang *, Kuang-Hui Li, Che-Hao Liao, Jose Manuel Taboada Vasquez, Chuanju Wang, Na Xiao, Xiaohang Li *

King Abdullah University of Science and Technology (KAUST), Advanced Semiconductor Laboratory, Thuwal 23955, Saudi Arabia

ABSTRACT

Compared to the vacuum-required deposition techniques, the chemical solution deposition (CSD) technique is superior in terms of low cost and ease of cation adjustment and upscaling. In this work, highly epitaxial indium- and aluminum-doped Ga_2O_3 thin films are deposited using a novel CSD technique. The 2θ, rocking curve, and φ-scan modes of x-ray diffraction (XRD) measurements and high-resolution transmission electron microscopy suggest that these thin films have a pure beta phase with good in- and out-of-plane crystallization qualities. The effect of incorporating indium and aluminum into the crystallization process is studied using high-temperature in situ XRD measurements. The results indicate that indium and aluminum doping can shift the crystallization of the thin films to lower and higher temperatures, respectively. Additionally, ultraviolet-visible spectroscopy measurements indicate that the bandgap of the sintered thin films can be tuned from 4.05 to 5.03 eV using a mixed precursor solution of In:Ga = 3:7 and Al:Ga = 3:7. The photodetectors based on the $(InGa)_2O_3$, pure Ga_2O_3, and $(AlGa)_2O_3$ samples exhibit the maximum photocurrents at 280, 255, and 230 nm, respectively. The results suggest that the described CSD technique is promising for producing high-quality bandgap tunable deep-ultraviolet photoelectrical and high-power devices.

1. Introduction

Gallium oxide (Ga_2O_3), an emerging ultra-wide bandgap (4.9 eV) group III oxide semiconductor material, has been intensively studied recently due to its potential applications in such fields as solar-blind photodetectors (PDs), gas sensors, field-effect transistors, luminescent phosphors, and photocatalysts. [1–5] In addition, Ga_2O_3 has five identified polymorphs, including rhombohedral (α), monoclinic (β), cubic (γ), and orthorhombic (ε) phases. [6–8] Among them, the monoclinic β-Ga_2O_3 exhibits the best chemical and thermal stability, making it the most promising candidate for actual applications compared to the other phases. [9] Given that the physical properties of β-Ga_2O_3 are highly anisotropic, the epitaxial growth of highly oriented epitaxial β-Ga_2O_3 thin film is essential to acquiring high-quality electronic devices. [2,9]

Today, single-crystalline β-Ga_2O_3 thin films can be routinely grown using various vacuum deposition techniques, including molecular beam epitaxy (MBE), chemical vapor deposition (CVD), pulsed laser deposition (PLD), and metal-organic vapor phase epitaxy. [10–13] Compared to such vacuum techniques, chemical solution deposition (CSD) is

superior in terms of low cost and ease of cation adjustment and upscaling [14–18]. However, to the best of our knowledge, the reported CSD-derived β-Ga_2O_3 thin films all remain polycrystalline with random orientations, [19–26] which may severely hinder the further development of the CSD technique in the future.

Furthermore, In_2O_3 and Al_2O_3 are two important members of the group III oxide semiconductor materials, with bandgaps of 3.5 and 8.6 eV, respectively. Therefore, incorporating indium (In) and aluminum (AL) into Ga_2O_3 to form $(In_xGa_{1-x})_2O_3$ and $(Al_xGa_{1-x})_2O_3$ alloys can broaden the bandgap range of the materials and enrich their ultraviolet (UV) applications (from 144 to 354 nm). However, In_2O_3 and Al_2O_3 are intrinsically stable in cubic and trigonal phases, respectively, different from the monoclinic β-Ga_2O, which causes additional difficulties in acquiring highly oriented epitaxial β-$(In_xGa_{1-x})_2O_3$ and β-$(Al_xGa_{1-x})_2O_3$ thin films compared to pure β-Ga_2O_3.

Such highly oriented epitaxial group III alloyed oxide thin films have been achieved via the mentioned vacuum deposition techniques. For instance, Zhang et al. and Liao et al. demonstrated the growth of highly oriented epitaxial β-$(In_{0.16}Ga_{0.84})_2O_3$ using the PLD technique. Liao

---

* Corresponding authors.
  E-mail addresses: xiao.tang@kaust.edu.sa (X. Tang), xiaohang.li@kaust.edu.sa (X. Li).
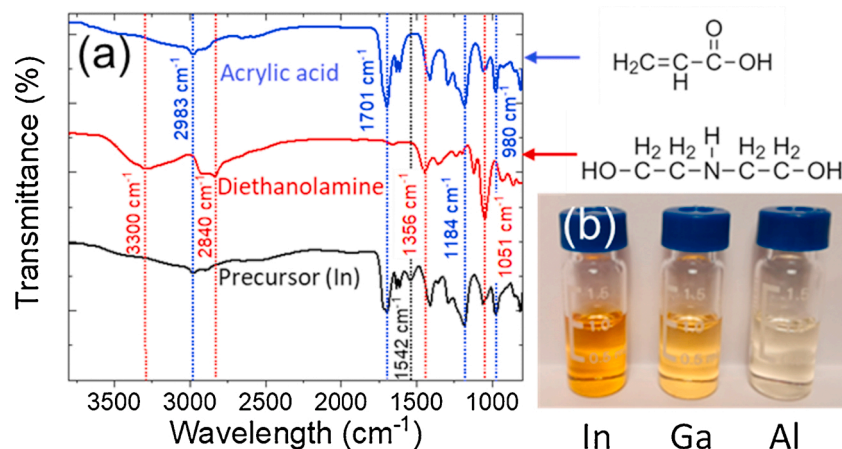
Fig. 1. (a) Fourier transform infrared spectra of the acrylic acid, diethanolamine, and indium precursor solution. (b) Image of indium, gallium, and aluminum precursor solutions.

et al. presented the growth of highly oriented epitaxial β-(Al$_{0.72}$Ga$_{0.18}$)$_2$O$_3$ using a PLD-post annealing combined technique. [27,28] Moreover, MBE and metal-organic CVD are promising techniques to achieve highly oriented epitaxial (In$_{0.35}$Ga$_{0.65}$)$_2$O$_3$ and (Al$_{0.52}$Ga$_{0.48}$)$_2$O$_3$ thin films, respectively. [29,30] However, such highly oriented epitaxial group III alloyed oxide thin films have never been successfully grown using the nonvacuum-required CSD technique because the quality control of the CSD-derived pure β-Ga$_2$O$_3$ thin films remains challenging.

In this paper, we describe a versatile and low-toxicity CSD technique for the epitaxial growth of group III oxide semiconductor thin films using low-cost acrylic acid and diethanolamine solvent mixtures. In the recipe, the group III nitrates, including In(NO$_3$)$_3$, Ga(NO$_3$)$_3$, and Al(NO$_3$)$_3$, are soluble in the mixed solvent. Therefore, the cation-to-cation ratio can be adjusted freely during the precursor preparation for specifically desired (In$_x$Ga$_{1-x}$)$_2$O$_3$ or (Al$_x$Ga$_{1-x}$)$_2$O$_3$ alloys. We chose (In$_{0.3}$Ga$_{0.7}$)$_2$O$_3$ and (Al$_{0.3}$Ga$_{0.7}$)$_2$O$_3$ as the representative samples to examine the crystal quality and growth mechanism of the In-Ga and Al-Ga alloyed oxide thin films. The x-ray diffraction (XRD) and transmission electron microscopy (TEM) analyses demonstrate that the deposited alloyed thin films have good crystal quality. High-temperature XRD measurements reveal that the crystallization temperature of the thin films shifts to lower and higher temperatures when adding In and Al content, respectively. Additionally, the ultraviolet-visible (UV–vis) spectroscopy measurements indicate that the bandgap of the sintered thin films can be tuned from 4.05 to 5.03 eV using the mixed precursor solution of In:Ga = 3:7 and Al:Ga = 3:7. The In-Ga and Al-Ga alloyed thin films are fabricated into PDs and have the highest photocurrent at 280 nm and 230 nm, respectively. Overall, the results suggest the promise of employing such a CSD technique to grow high-quality bandgap tunable deep-ultraviolet (DUV) photoelectrical devices.

2. Experiment

2.1. Precursor solution

The precursor solution was prepared by dissolving 1 mmol of individual metal nitrate into 2 mL of acrylic acid with vigorous stirring at 40℃. After 2 h of reaction, 100 u L diethanolamine was added to the solution. After stirring for another 1 h, the precursor solution was ready for use. The In, Ga, and Al precursor solutions are presented in Fig. 1(b). The precursor solution for alloyed oxide thin films was prepared in the last step by mixing the In, Ga, and Al solution with vigorous stirring at the desired stoichiometric ratio.

2.2. Thin film

The precursor solution was spin-coated on a 1 cm × 1 cm sapphire substrate at a rotating speed of 3000 rpm for 1 min. After each single-layer coating, the sample was placed on a heating plate at 310 °C and held for 5 min. The coating-heating step was repeated three times. Afterward, the precursor-coated thin films were placed in a muffle furnace. The furnace was heated to 1100 °C – 1500 °C at a ramping rate of 10 °C/min. After holding at the target temperature for 2 h, the furnace was naturally cooled. During sintering, the Al-Ga alloyed sample was covered by another 1 cm × 1 cm sapphire substrate to avoid the sublimation of Ga.

2.3. Characterization

The Fourier transform infrared spectroscopy of the precursor solution was measured using a Bruker Tensor 27 spectrometer. The material phases, in- and out-of-plane quality, and high-temperature in situ phase evolution of the thin films were measured using a g Bruker D8 Advance XRD with Cu Kα radiation (λ = 1.5406 Å). The surface morphology of the thin films was investigated using a Supra 35 scanning electron microscope. The high-resolution (HR) TEM lamella of the thin-film samples was prepared using an FEI Helios G4 dual-beam focused ion beam scanning electron microscope system with a Ga source and omni-probe. The HR-TEM images and fast Fourier transform (FFT) patterns of the interfaces were obtained on an HR-TEM system (Titan ST microscope; FEI, USA) with an operating voltage of 300 keV. The UV–vis measurements were performed using a Lambda 950 UV/Vis/NIR spectrophotometer from PerkinElmer. The photoelectrical characteristics were measured using a Zolix DSR600-X150−200-UV automated spectroradiometric measurement system.

3. Results and discussion

The Fourier transform infrared spectrum of the indium precursor solution, representing all three metal precursor solutions, and the pure acrylic acid and pure diethanolamine as a reference are illustrated in Fig. 1(a). Moreover, a picture for the three metal precursor solutions, In, Ga, and Al, is depicted in Fig. 1(b). The signals from the In precursor solution were identified by reference from the spectrum of the pure acrylic acid and diethanolamine. The ratio between diethanolamine and acrylic acid in the precursor solution is 1:20, and the cation concentration is as low as 0.5 M; thus, most peaks in the mixed precursor solution are from acrylic acid. As noted in the spectrum, the peaks at 2983, 1701, 1184, and 980 cm^{-1} originate from the O—H stretching, CO stretching, CO stretching, and CC══─══ vibration of acrylic acid,
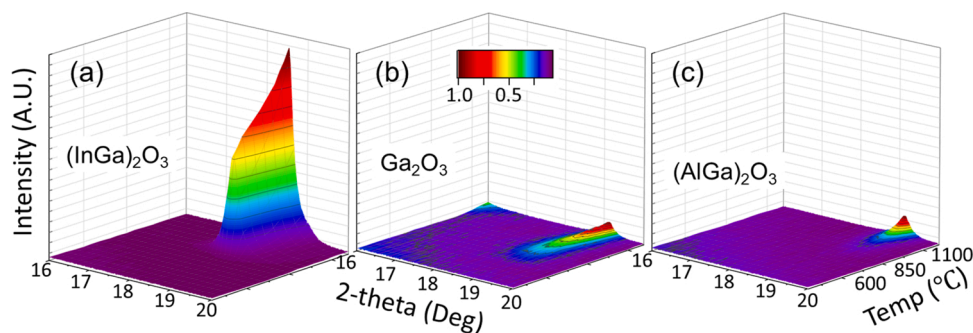
Fig. 2. High-temperature in situ 2θ X-ray diffraction spectrum from 16 ° to 20 ° measured on (a) $(InGa)_2O_3$, (b) Ga_2O_3, and (c) $(AlGa)_2O_3$ precursor thin films from 400℃ to 1200℃ with a temperature interval of 50℃. All images are plotted using the same intensity scale, 2θ, and temperature. Colors represent the relative intensity normalized by the maximum value for each sample.

Table 1
Ionic radii, electronegativity, and Pauling bond strengths for In—O, GaO, and Al——O bonds.

Bond	Ionic radii (Å)	Electronegativity of cation	Pauling bond strengths
IN—O	2.19–2.20	1.7	0.57
Ga—O	1.89–1.94	1.6	0.61
Al—O	1.74–1.93	1.5	0.65

respectively. The peak at 1051 cm^{-1} is assigned to the C—N stretching of diethanolamine. The peak at 1542 cm^{-1} is assigned to the N–O stretching of NO_3^-.

The spin-coated precursor thin-film samples are subjected to a course of high-temperature in situ XRD measurements from 400℃ to 1200℃, as displayed in Fig. 2. The scans are focused on a narrowed range from 16 ° to 20 ° to avoid long-term scanning that could interfere with the nucleation and growth process of the samples. For all samples, only the diffraction peak corresponding to β-Ga_2O_3 (-201) was observed in the 2θ range, and all peak intensities increased with the reaction temperature. Interestingly, throughout the measurements, the peak intensity of (-201) for the samples is in the order $(InGa)_2O_3 > Ga_2O_3 > (AlGa)_2O_3$, implying that In and Al may facilitate and postpone the crystallization of Ga_2O_3.

The influence of In and Al doping can be understood in terms of grain growth kinetics during a solid-state reaction. [31] By incorporating In and Al into the Ga_2O_3 thin films, the Ga—O bonds are believed to be partially replaced by the In—O and AlO— bonds, respectively. The Pauling bond strengths can be calculated based on the average Pauling scale of electronegativity of the involved elements using the following equation [32]:

$$P_{AB} = 1 - exp\left[-\frac{1}{4}(X_A - X_B)\right],$$

where P_{AB} is the Pauling bond strength, and X_A and X_B are the average electronegativity of the cations and anions, respectively. Based on the calculation, the ionic radii, electronegativity, and Pauling bond strengths for the In—O, GaO, and AlO—— bonds are listed in Table 1. As evidenced from the calculation, In—O and AlO— have a relatively lower and higher Pauling bond strength compared to Ga—O. Hence, either a loose or tight bonding structure occurs in the vicinity of the doping centers. In addition, In induces a loose bonding structure for the $(InGa)_2O_3$ sample, facilitating the crystallization procedure in the solid-state reaction, whereas Al plays an opposite role for the $(AlGa)_2O_3$ sample.

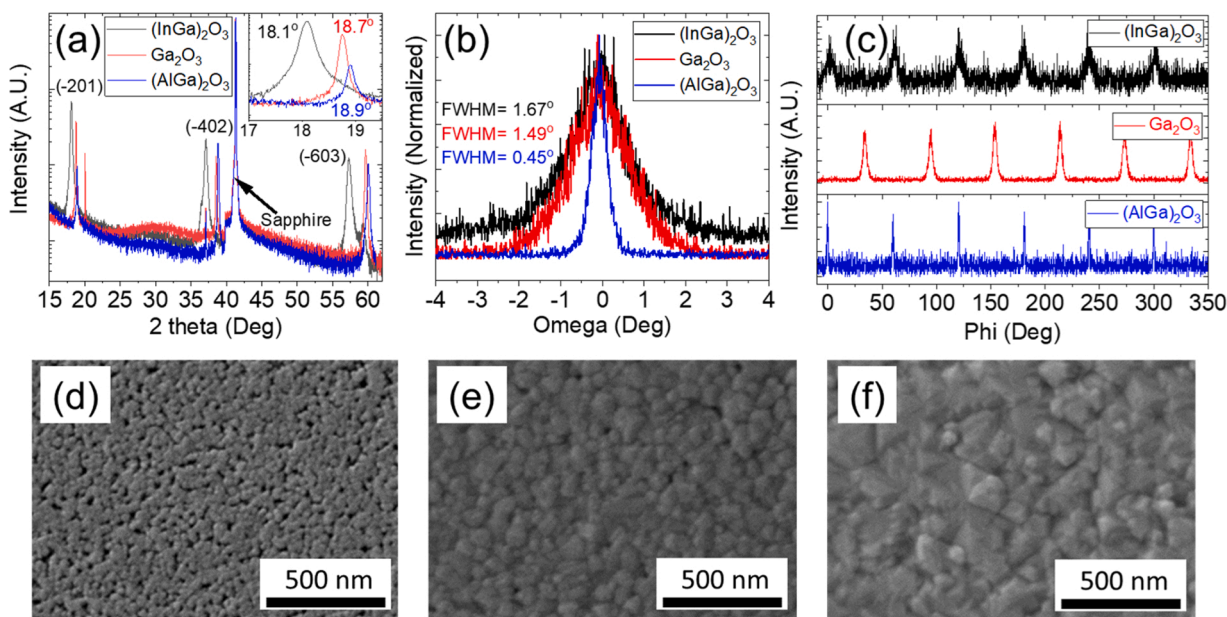Based on the information provided by the high-temperature in situ

Fig. 3. (a) 2θ X-ray diffraction patterns, (b) rocking curve of (-201) reflection, and (c) φ-scan of (-401) plane measured on the $(InGa)_2O_3$ (black), Ga_2O_3 (red), and $(AlGa)_2O_3$ (blue) thin-film samples. Scanning electron microscopy images on (d) $(InGa)_2O_3$, (e) Ga_2O_3, and (f) $(AlGa)_2O_3$ thin-film samples (For interpretation of the references to colour in this figure legend, the reader is referred to the web version of this article).
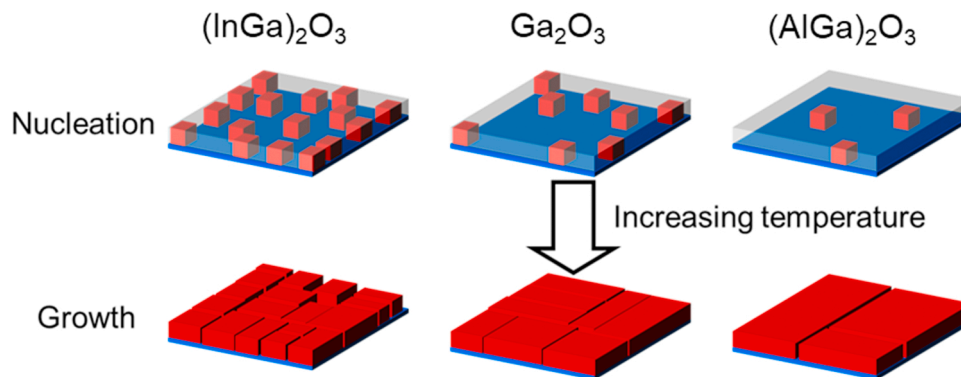
Fig. 4. Nucleation-growth modes for the (InGa)$_2$O$_3$, Ga$_2$O$_3$, and (AlGa)$_2$O$_3$ thin films.

XRD measurements, in the actual deposition procedure, the (InGa)$_2$O$_3$ and Ga$_2$O$_3$ thin films are sintered at 1100℃, whereas the (AlGa)$_2$O$_3$ thin film is sintered at 1500℃ because the Al content significantly postpones the crystallization. Fig. 3 illustrates the 2θ XRD patterns (a), rocking curve of (-201) reflection (b), and φ-scan of the (-401) plane (c) measured on the (InGa)$_2$O$_3$ (black), Ga$_2$O$_3$ (red), and (AlGa)$_2$O$_3$ (blue) thin-film samples. In the 2θ spectra, for all three samples, only the diffraction peaks from the $\{\overline{2}\,01\}$ planes of the beta phase were observed, whereas the diffraction peaks from the random orientation of the grains (e.g., β-Ga$_2$O$_3$ (400) at approx. 30 °) were absent. [33] The results indicate that all thin films are crystallized along a single preferred orientation without phase separation potentially induced by the In and Al incorporation. Importantly, expansion and compression of the unit cells are observed due to the incorporation of In and Al atoms, which are larger and smaller than Ga, respectively, as listed in Table 1. This activity is evidenced from the inset of Fig. 3(a), in which the (-201) diffraction peak shifted from 18.7 ° to 18.1 ° and 18.9 ° after doping with In and Al, respectively.

The rocking curve measurements indicate that (AlGa)$_2$O$_3$ has a dramatically decreased full width at half maximum (FWHM) value of only 0.45 ° compared to (InGa)$_2$O$_3$ (1.67 °) and Ga$_2$O$_3$ (1.49 °) thin films. In contrast, the (InGa)$_2$O$_3$ thin film exhibits a broadening peak in both the 2θ and rocking curve scanning modes. The results indicate that the grain size of the samples is in the order (AlGa)$_2$O$_3$ > Ga$_2$O$_3$ > (InGa)$_2$O$_3$. The scanning electron microscopy (SEM) images are measured on the three samples to obtain an intuitive view of the morphology, as demonstrated in Fig. 3(d-f). Compared to the pure Ga$_2$O$_3$ sample, the (InGa)$_2$O$_3$ sample represents a wrinkled and porous surface; in contrast, the continuity and grain size of the (AlGa)$_2$O$_3$ sample are significantly enhanced. The SEM results correspond quite well with the XRD patterns.

The thin-film samples are also annealed at 1300℃ for 3 h to further

verify such a phenomenon. The rocking curve, φ-scan, and SEM images of the samples are displayed in the supporting information (Figure S1). The FWHM values of the rocking curve for (InGa)$_2$O$_3$, Ga$_2$O$_3$, and (AlGa)$_2$O$_3$ are 1.25 °, 1.13 °, and 0.8 °, respectively. The average FWHM values of the peaks in the φ-scan for (InGa)$_2$O$_3$, Ga$_2$O$_3$, and (AlGa)$_2$O$_3$ are 6.69 °, 6.25 °, and 4.8 °, respectively. Moreover, larger grains are also observed on the SEM image of the (AlGa)$_2$O$_3$ compared to the other two samples. The grain size difference between the three samples can be explained via the classical nucleation-growth mechanism. [34] During the solid-state crystallization process, nucleation and growth occur simultaneously in a competitive relationship [34] and are favored at lower and higher temperatures, respectively.

For the Ga$_2$O$_3$ sample, when the temperature ramped to the nucleation onset, several nuclei form at the interface of the Ga$_2$O$_3$/sapphire interface. With further temperature increases, the already-formed nuclei serve as the crystallization front and grow into larger grains in consuming the amorphous Ga$_2$O$_3$ content in its vicinity. Second, for the (InGa)$_2$O$_3$ sample, due to the facilitation effect of In on the crystallization, a larger number of nuclei is formed when the nucleation onset is reached. Later, when the temperature further increases, the nuclei grow by consuming the vicinal amorphous content and coarsening with the neighboring nuclei. In this understanding, the small grain size of the (InGa)$_2$O$_3$ sample could occur for two reasons. First, the surface free energy for the nuclei is higher than in the amorphous phase; therefore, the atom diffusion and, thus, the grain growth are more favored in the Ga$_2$O$_3$ sample. Second, as more precursor content is consumed in the nucleation stage, the materials for grain growth are relatively limited in the (InGa)$_2$O$_3$ sample. Eventually, the (InGa)$_2$O$_3$ sample contains a larger number of grains with a smaller size. For the (AlGa)$_2$O$_3$ sample, the onset temperature is dramatically elevated by aluminum doping; hence, the nucleation is largely limited during the ramping of the temperature. When crystallization is triggered at a high temperature, the
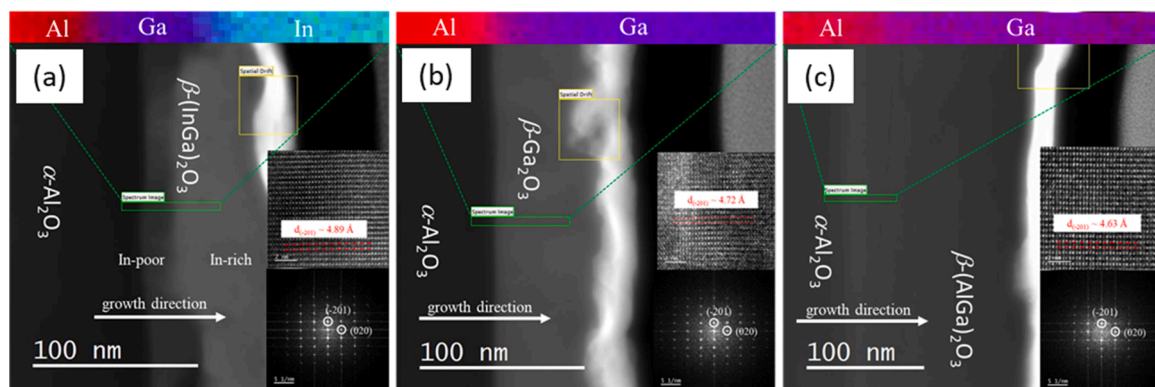

Fig. 5. Cross-sectional high-resolution transmission electron microscopy image, elemental mapping, regional magnified image, and fast Fourier transform pattern obtained on the (a) (InGa)$_2$O$_3$, (b) Ga$_2$O$_3$, and (c) (AlGa)$_2$O$_3$ thin-film samples.
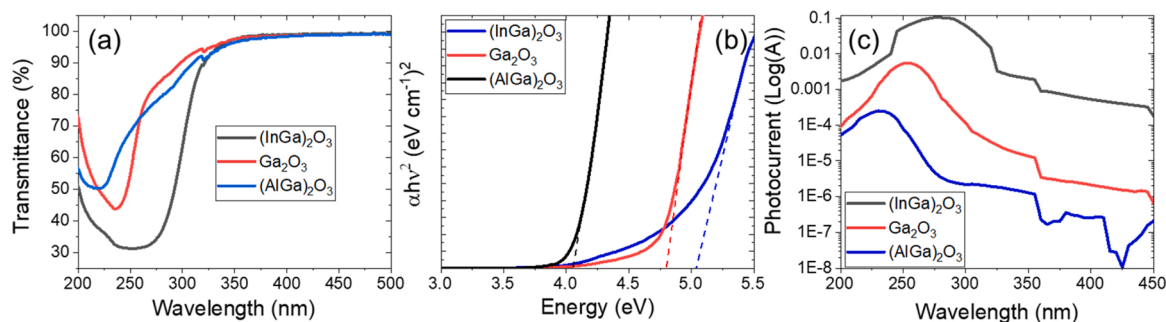
Fig. 6. (a) Transmittance spectrum and (b) Tauc plot of $(\alpha h\nu)^2$ as a function of the photon energy for $(InGa)_2O_3$, Ga_2O_3, and $(AlGa)_2O_3$ thin films. (c) Wavelength-dependent photocurrent of the corresponding photodetectors.

amorphous phase is consumed by the growth of a very limited number of nuclei, eventually resulting in a smaller number of grains with a larger size. Based on the above descriptions, the nucleation-growth modes for $(InGa)_2O_3$, Ga_2O_3, and $(AlGa)_2O_3$ thin films are illustrated in Fig. 4.

In addition, the φ-scan reveals that all three samples have hexagonal-like atom frameworks in their (-401) plane, suggesting they all have a monoclinic beta phase with good out-of-plane crystal orientation. Again, in the φ-scan, the broadening and narrowing of the peaks were observed on the $(InGa)_2O_3$ and $(AlGa)_2O_3$ samples, consistent with the observations in 2θ and rocking curve measurements.

Fig. 5 presents the cross-sectional HR-TEM images, elemental mappings, and FFT patterns of the $(InGa)_2O_3$, Ga_2O_3, and $(AlGa)_2O_3$ thin-film samples. First, the cross-sectional images reveal that the thicknesses for $(InGa)_2O_3$, Ga_2O_3, and $(AlGa)_2O_3$ thin films are around 70, 60, and 140 nm, respectively. The thickness differences between the samples could originate from the different amounts of crystalized water in the metal nitrate precursor salts. The water content can largely affect the wetting property of the precursor solution and, thus, the final thickness of the sintered thin films. As evidenced from the magnified HR-TEM images and corresponding FFT patterns, the preferential growth of {-201} β-Ga_2O_3 occurs on the (0001) sapphire plane, indicating a high crystallinity for all three samples. The expansion and compression of the unit cells due to the incorporation of In and Al atoms into the Ga_2O_3 lattice are observed. The interplane spacing of the {-201} planes is 4.89 Å, 4.72 Å, and 4.63 Å for the $(InGa)_2O_3$, Ga_2O_3, and $(AlGa)_2O_3$ samples, respectively. This result corresponds well to the 2θ XRD results.

Moreover, elemental mapping indicates that the $(InGa)_2O_3$ thin-film sample has an In-poor region at the $(InGa)_2O_3$/interface and an In-rich region at the upper layer close to the thin-film surface. Such a phenomenon is the reason for the sublimation of In due to the higher saturated vapor pressure of In compared to Ga. During deposition at a high temperature in a vacuum atmosphere, In tends to evaporate from the $(InGa)_2O_3$ interface to the surface of the thin films and eventually aggregates at the upper part of the layer.

To examine the potential of the CSD technique for producing bandgap tunable DUV photoelectrical devices, the optical bandgaps of the $(InGa)_2O_3$, Ga_2O_3, and $(AlGa)_2O_3$ thin-film samples are subjected to the UV–vis measurements, as presented in Fig. 6(a). The bandgaps are 4.05, 4.8, and 5.03 eV, respectively, using the Tauc plot of $(\alpha h\nu)^2$ as a function of the photon energy, as displayed in Fig. 6(b). Moreover, the samples were also fabricated onto PDs by depositing Ti/Au contacts onto the thin-film surface. The photocurrent of the devices was measured under an excitation light ranging from 200 to 500 nm at a fixed bias voltage of 5 V, as depicted in Fig. 6(c).

First, the PDs based on the $(InGa)_2O_3$, Ga_2O_3, and $(AlGa)_2O_3$ thin films have photocurrent peaks at 280, 255, and 230 nm, respectively. The photocurrent peak shift is due to the intrinsic bandgaps for In_2O_3, Ga_2O_3, and Al_2O_3, which are 3.5, 4.9, and 8.6 eV, respectively. The alloying of Ga_2O_3 with In_2O_3 and Al_2O_3 can make the maximum photoresponse red- and blue-shifted, respectively. Second, the photocurrent

for the devices is in the order $(InGa)_2O_3 > Ga_2O_3 > (AlGa)_2O_3$. A similar phenomenon was observed in some previous reports and can be the reason for the electron-phonon coupling dependence of the carrier mobility. Stronger electron-phonon coupling results in lower carrier mobility. [35–37] The electron-phonon coupling is believed to be proportional to the ionic strength [36]. Therefore, based on the ionic strength in Table 1, In and Al doping can increase and decrease the carrier mobility and, hence, the photocurrent of the PDs, respectively.

4. Conclusion

In summary, highly epitaxial $(InGa)_2O_3$, Ga_2O_3, and $(AlGa)_2O_3$ thin films are deposited on sapphire using a novel CSD technique. The 2θ, rocking curve, and φ-scan modes of XRD measurements and the HR-TEM suggest that the thin films have a pure beta phase, with good in- and out-of-plane crystallization qualities. The high-temperature in situ XRD measurements indicate that In and Al doping can shift the crystallization of the thin films to a lower and higher temperature, respectively, possibly resulting in relatively smaller and larger grains in $(InGa)_2O_3$ and $(AlGa)_2O_3$ thin films, respectively. The UV–vis spectroscopy measurements indicate that the bandgap of the sintered thin films can be tuned from 4.05 to 5.03 eV using the mixed precursor solution of In:Ga = 3:7 and Al:Ga = 3: 7. The thin films are fabricated into PDs and have maximum photocurrents at 280, 255, and 230 nm for $(InGa)_2O_3$, Ga_2O_3, and $(AlGa)_2O_3$ thin films, respectively. Overall, the CSD technique described in this work is demonstrated as a low-cost, easily scaled-up technique for producing high-quality bandgap tunable DUV photoelectrical devices.

Declaration of Competing Interest

The authors declare that they have no known competing financial interests or personal relationships that could have appeared to influence the work reported in this paper.

Appendix A. Supplementary data

Supplementary material related to this article can be found, in the online version, at doi:https://doi.org/10.1016/j.jeurceramsoc.2021.09.064.

References

[1] M. Rebien, W. Henrion, M. Hong, J.P. Mannaerts, M. Fleischer, Optical properties of gallium oxide thin films, Appl. Phys. Lett. 81 (2002) 250–252.

[2] S.J. Pearton, J. Yang, P.H. Cary, F. Ren, J. Kim, M.J. Tadjer, M.A. Mastro, A review of Ga2O3 materials, processing, and devices, Appl. Phys. Rev. 5 (2018).

[3] Y. Wang, K. Xu, D. Li, H. Zhao, Z. Hu, Persistent luminescence and photocatalytic properties of Ga2O3:Cr3+, Zn2+ phosphors, Opt. Mater. (Amst) 36 (2014) 1798–1801.

[4] P. Castro-Fernández, D. Mance, C. Liu, I.B. Moroz, P.M. Abdala, E.A. Pidko, C. Copéret, A. Fedorov, C.R. Müller, Propane dehydrogenation on Ga2O3-based catalysts: contrasting performance with coordination environment and acidity of surface sites, ACS Catal. 11 (2021) 907–924.

[5] L. Mazeina, F.K. Perkins, V.M. Bermudez, S.P. Arnold, S.M. Prokes, Functionalized Ga2O3 nanowires as active material in room temperature capacitance-based gas sensors, Langmuir 26 (2010) 13722–13726.

[6] J.E.N. Swallow, C. Vorwerk, P. Mazzolini, P. Vogt, O. Bierwagen, A. Karg, M. Eickhoff, J. Schörmann, M.R. Wagner, J.W. Roberts, P.R. Chalker, M.J. Smiles, P. Murgatroyd, S.A. Razek, Z.W. Lebens-Higgins, L.F.J. Piper, L.A.H. Jones, P. K. Thakur, T.-L. Lee, J.B. Varley, J. Furthmüller, C. Draxl, T.D. Veal, A. Regoutz, Influence of polymorphism on the electronic structure of Ga2O3, Chem. Mater. 32 (2020) 8460–8470.

[7] S. Yoshioka, H. Hayashi, A. Kuwabara, F. Oba, K. Matsunaga, I. Tanaka, Structures and energetics of Ga2O3 polymorphs, J. Phys. Condens. Matter 19 (2007).

[8] I. Cora, F. Mezzadri, F. Boschi, M. Bosi, M. Čaplovičová, G. Calestani, I. Dódony, B. Pécz, R. Fornari, The real structure of ε-Ga2O3 and its relation to κ-phase, CrystEngComm 19 (2017) 1509–1516.

[9] S.J. Hao, M. Hetzl, F. Schuster, K. Danielewicz, A. Bergmaier, G. Dollinger, Q.L. Sai, C.T. Xia, T. Hoffmann, M. Wiesinger, S. Matich, W. Aigner, M. Stutzmann, Growth and characterization of β-Ga2O3 thin films on different substrates, J. Appl. Phys. 125 (2019).

[10] Z. Liu, Y. Zhi, S. Li, Y. Liu, X. Tang, Z. Yan, P. Li, X. Li, D. Guo, Z. Wu, W. Tang, Comparison of optoelectrical characteristics between Schottky and Ohmic contacts to β-Ga2O3 thin film, J. Phys. D Appl. Phys. 53 (2020).

[11] K.H. Li, N. Alfaraj, C.H. Kang, L. Braic, M.N. Hedhili, Z. Guo, T.K. Ng, B.S. Ooi, Deep-ultraviolet photodetection using single-crystalline beta-Ga2O3/NiO heterojunctions, ACS Appl. Mater. Interfaces 11 (2019) 35095–35104.

[12] E.G. Víllora, K. Shimamura, K. Kitamura, K. Aoki, Rf-plasma-assisted molecular-beam epitaxy of β-Ga2O3, Appl. Phys. Lett. 88 (2006).

[13] K. Uno, M. Ohta, I. Tanaka, Growth mechanism of α-Ga2O3 on a sapphire substrate by mist chemical vapor deposition using acetylacetonated gallium source solutions, Appl. Phys. Lett. 117 (2020).

[14] Q.X. Jia, T.M. McCleskey, A.K. Burrell, Y. Lin, G.E. Collis, H. Wang, A.D. Li, S. R. Foltyn, Polymer-assisted deposition of metal-oxide films, Nat. Mater. 3 (2004) 529–532.

[15] H.S. Jeon, M.S. Jee, H. Kim, S.J. Ahn, Y.J. Hwang, B.K. Min, Simple chemical solution deposition of Co(3)O(4) thin film electrocatalyst for oxygen evolution reaction, ACS Appl. Mater. Interfaces 7 (2015) 24550–24555.

[16] A.K. Burrell, T. Mark McCleskey, Q.X. Jia, Polymer assisted deposition, Chem. Commun. (Camb.) (2008) 1271–1277.

[17] N. Park, K. Sun, Z. Sun, Y. Jing, D. Wang, High efficiency NiO/ZnO heterojunction UV photodiode by sol–gel processing, J. Mater. Chem. C 1 (2013).

[18] X. Tang, Y. Zhao, W. Wu, N.H. Andersen, J.C. Grivel, High-Jc YBa2Cu3O7−x-Ag superconducting thin films synthesized through a fluorine-free MOD method, J. Eur. Ceram. Soc. 35 (2015) 1761–1769.

[19] Y. Kokubun, K. Miura, F. Endo, S. Nakagomi, Sol-gel prepared β-Ga2O3 thin films for ultraviolet photodetectors, Appl. Phys. Lett. 90 (2007).

[20] G.S. Cai, Y.L. Pei, S.D. Zhang, Investigation of solution-processed Ga2O3 thin films and their application in dielectric materials, Mater. Sci. Forum 1014 (2020) 27–32.

[21] Y. Ohya, Y. Okano, Y. Kasuya, Takayuki. B, Fabrication of Ga2O3 thin films by aqueous solution deposition, J. Ceram. Soc. Jpn. 117 (1369) (2009) 973–977.

[22] M. Bartic, M. Ogita, M. Isai, C.-L. Baban, H. Suzuki, Oxygen sensing properties at high temperatures of β-Ga2O3 thin films deposited by the chemical solution deposition method, J. Appl. Phys. 102 (2007).

[23] L. Li, W. Wei, M. Behrens, Synthesis and characterization of α-, β-, and γ-Ga2O3 prepared from aqueous solutions by controlled precipitation, Solid State Sci. 14 (2012) 971–981.

[24] L.B. Cheah, R.A.M. Osman, P. Poopalan, Ga2O3 thin films by sol-gel method its optical properties, The 2nd International Conference on Applied Photonics and Electronics 2019 (InCAPE 2019) (2020).

[25] H. Shen, Y. Yin, K. Tian, K. Baskaran, L. Duan, X. Zhao, A. Tiwari, Growth and characterization of β-Ga2O3 thin films by sol-gel method for fast-response solar-blind ultraviolet photodetectors, J. Alloys. Compd. 766 (2018) 601–608.

[26] W. Xu, H. Cao, L. Liang, J.B. Xu, Aqueous solution-deposited gallium oxide dielectric for low-temperature, low-operating-voltage indium oxide thin-film transistors: a facile route to green oxide electronics, ACS Appl. Mater. Interfaces 7 (2015) 14720–14725.

[27] F. Zhang, K. Saito, T. Tanaka, M. Nishio, Q. Guo, Wide bandgap engineering of (GaIn)2O3 films, Solid State Commun. 186 (2014) 28–31.

[28] C.-H. Liao, K.-H. Li, C.G. Torres-Castanedo, G. Zhang, X. Li, Wide range tunable bandgap and composition β-phase (AlGa)2O3 thin film by thermal annealing, Appl. Phys. Lett. 118 (2021).

[29] T. Oshima, S. Fujita, Properties of Ga2O3-based (InxGa1-x)2O3 alloy thin films grown by molecular beam epitaxy, Physica Status Solidi (c) 5 (2008) 3113–3115.

[30] A.F.M. Anhar Uddin Bhuiyan, Z. Feng, J.M. Johnson, H.-L. Huang, J. Hwang, H. Zhao, MOCVD epitaxy of ultrawide bandgap β-(AlxGa1−x)2O3 with high-Al composition on (100) β-Ga2O3 substrates, Cryst. Growth Des. 20 (2020) 6722–6730.

[31] I. Bretos, R. Jimenez, J. Ricote, M.L. Calzada, Low-temperature crystallization of solution-derived metal oxide thin films assisted by chemical processes, Chem. Soc. Rev. 47 (2018) 291–308.

[32] K. Singh, S.A. Acharya, S.S. Bhoga, Low temperature processing of dense samarium-doped CeO2 ceramics: sintering and intermediate temperature ionic conductivity, Ionics 13 (2007) 429–434.

[33] D. Guo, Y. Su, H. Shi, P. Li, N. Zhao, J. Ye, S. Wang, A. Liu, Z. Chen, C. Li, W. Tang, Self-powered ultraviolet photodetector with superhigh photoresponsivity (3.05 A/W) based on the GaN/Sn:Ga2O3 pn Junction, ACS Nano 12 (2018) 12827–12835.

[34] D. Savytskii, B. Knorr, V. Dierolf, H. Jain, Demonstration of single crystal growth via solid-solid transformation of a glass, Sci. Rep. 6 (2016) 23324.

[35] N. Ma, N. Tanen, A. Verma, Z. Guo, T. Luo, H. Xing, D. Jena, Intrinsic electron mobility limits in β-Ga2O3, Appl. Phys. Lett. 109 (2016).

[36] J. Zhang, J. Shi, D.-C. Qi, L. Chen, K.H.L. Zhang, Recent progress on the electronic structure, defect, and doping properties of Ga2O3, APL Mater. 8 (2020).

[37] T. Oshima, Y. Kato, N. Kawano, A. Kuramata, S. Yamakoshi, S. Fujita, T. Oishi, M. Kasu, Carrier confinement observed at modulation-doped β-(AlxGa1−x)2O3/Ga2O3 heterojunction interface, Appl. Phys. Express 10 (2017).